Chemical and microstructural characterisation of HfO2-Y2O3 ceramics with high amount of Y2O3 (33, 40 and 50 mol. %) manufactured using spark plasma sintering

Lisa Audouard, Maria Tsoutsouva, Nicolas Horezan, Etienne Rimpot, Jean-Francois Justin, Pierre Bertrand, Cécile Langlade, Matthieu Garcia, Aurélie Julian-Jankowiak

To cite this version:

Lisa Audouard, Maria Tsoutsouva, Nicolas Horezan, Etienne Rimpot, Jean-Francois Justin, et al.. Chemical and microstructural characterisation of HfO2-Y2O3 ceramics with high amount of Y2O3 (33, 40 and 50 mol. %) manufactured using spark plasma sintering. Journal of the European Ceramic Society, 2022, 43 (5), pp.2093-2103. 10.1016/j.jeurceramsoc.2022.12.061. hal-03945398

HAL Id: hal-03945398
https://hal.science/hal-03945398v1

Submitted on 26 Jan 2023

Chemical and microstructural characterisation of HfO_2-Y_2O_3 ceramics with high amount of Y_2O_3 (33, 40 and 50 mol. %) manufactured using spark plasma sintering

L. Audouard[a,b,c], M. G. Tsoutsouva[a], N. Horezan[a], E. Rimpot[a], J. F. Justin[a], P. Bertrand[b], C. Langlade[b], M. Garcia[c], A. Julian-Jankowiak[a]

[a] ONERA/DMAS, Châtillon, 92320 France
[b] Université de Bourgogne Franche-Comté, laboratoire ICB UMR CNRS-UB-UTBM 6303, 90010 Belfort France
[c] Direction des systèmes orbitaux, CNES, Toulouse, 31410, France

Abstract

Hafnia based ceramics are potential promising candidates to be used as thermal barrier coatings (TBC) for applications in the field of propulsion. In this study, Spark Plasma Sintering (SPS) of fully stabilised hafnia with yttrium oxide (yttria) was investigated to provide a better understanding of the effect of manufacturing parameters, on the crystallography, chemistry and microstructure of the material. Several hafnia powders, containing different amounts of yttria (33 mol. %, 40 mol. % or 50 mol. %), were sintered by SPS at different temperature levels ranging from 1600 to 1850 °C. On these materials, X-ray diffraction patterns associated with scanning electron micrographs have highlighted the influence of both the sintering temperature and the amount of yttria on the final composition, the lattice parameter and the microstructure of hafnia-based materials. In the end, it is established that, for all quantities of yttrium employed, the main phase is $Y_2Hf_2O_7$ with very high densification levels.

KEY WORDS: HfO_2-Y_2O_3 ceramics, $Y_2Hf_2O_7$, Fluorite, Spark Plasma Sintering (SPS), stabilisation

1. Introduction

For satellite propulsion, environmental regulations tend to limit the use of highly polluting and dangerous propellants (such as hydrazine) while improving the performance of thrusters. More specifically, operating temperatures are increased and materials development should withstand those requirements. To answer those requirements, ceramic/metal Functionally Graded Materials (FGM) are developed using Atmospheric Plasma Spraying (APS). Within the FMG, the ceramic acts as a Thermal Barrier Coating (TBC). The present study is focused on the optimisation of this ceramic as its composition has a huge influence on the resistance of the FGM system under harsh conditions. Thus, bulk ceramic materials are densified using Spark Plasma Sintering (this study) or natural sintering [1,2]. Among all the material solutions for ultra-high temperature / TBC applications, stabilised zirconia is commonly used [3–11]. Also, few studies demonstrate the ability of hafnia based materials to be used for this type of application [6,12–15]. However, both zirconia and hafnia present phase transitions [16], between the monoclinic (m), the tetragonal (t) and the cubic (c) systems. Those reversible allotropic transformations occur at 1700 °C (m $\rightleftharpoons$ t) and 2600 °C (t $\rightleftharpoons$ c) for hafnia [17] and at about 1170 °C (m $\rightleftharpoons$ t) and 2370 °C (t $\rightleftharpoons$ c) for zirconia [18]. These transitions, and more particularly the m $\rightleftharpoons$ t, induce huge dimensional variations [19], during heating and cooling, which have detrimental effects on the global structure scale. To overcome this effect, they are often stabilised with rare earth oxides, and particularly yttrium oxide (Y_2O_3).

Zirconia and hafnia are considered as twin oxides since they present similar crystalline structures and the ionic radii of Zr^{4+} and Hf^{4+} are very close, 0.84 Å and 0.83 Å respectively

[20]. However, hafnia is a bit more refractory than zirconia as its melting point is about 100 °C higher, its transition temperature, from the tetragonal to the monoclinic phase, is also 600 °C higher and it has a lower ionic conductivity. Those points justify the choice to investigate hafnia instead of zirconia in the present study that concerns ultra-high temperature applications. The stabilisation of these ceramics with rare earth oxides (RE_2O_3) induces the substitution of a cation Hf^{4+} by a cation RE^{3+}. The stabilisation of zirconia with low content yttria has been widely studied in the literature [6,21–28], but only few studies deal with HfO_2-based materials and their stabilisation with rare earth oxides (at low content). i.e. Y_2O_3 [29], Gd_2O_3 or Yb_2O_3 [30] but also Sm_2O_3, Dy_2O_3 [31] and Nd_2O_3, Er_2O_3 [32]. In all cases, to preserve the electro-neutrality of the structure, this phenomenon generates an oxygen deficient fluorite structure with the creation of oxygen vacancies [20]. Some oxides, such as CeO_2, ZrO_2, HfO_2, ThO_2, UO_2 or PuO_2 present an ideal fluorite structure [33] and some of them as CeO_2 and ZrO_2 are naturally ionic conductors.

In our previous study [1], HfO_2-Y_2O_3 ceramics, which were prepared by cold isostatic pressing and high temperature natural sintering, demonstrated promising results for high yttria content compositions. Especially, ionic conductivity was reduced by two decades at 500 °C and one decade at 900 °C for HfO_2 monoliths containing between 12 and 33 mol. % of Y_2O_3 which could be potentially interesting in developments for environmental barrier coating applications (EBC). The use of high content of rare earth oxide for the stabilisation of hafnia is not very common in the literature. Indeed, most of the data are dedicated to the stabilisation of hafnia with low yttria content (often around 8 mol. %) [34,35]. Zhu et al. [15] studied higher amounts of stabiliser (up to 25 mol. % of Y_2O_3). They highlighted that higher amounts of Y_2O_3 in HfO_2 led to a decrease in thermal conductivity, showing the importance of optimising the composition of HfO_2-Y_2O_3 ceramics to increase their performances for TBC applications.

In the present work, very high amounts (33 mol. %, 40 mol. % and 50 mol. %) of yttria are investigated, as they seemed promising to reduce both the thermal conductivity and the diffusion of charged species, such as O^{2-}. In addition, in the present study, we use an alternative sintering method for these materials: the Spark Plasma Sintering (SPS) process [36]. This innovative technique relies on a very high powder densification speed as the heating rates can reach several hundreds of degrees per minute. Moreover, pressing and sintering are performed simultaneously through the application of a uniaxial pressure and a high intensity current (several thousands of A). Consequently, this technique provides high densification rates with limited grain growth allowing the conservation of the powder particle size. These features are beneficial to obtain denser materials with better mechanical properties and higher oxidation resistance, compared to the materials produced by natural sintering. However, this sintering process is also often responsible for carbon contamination [37], material reduction and segregation of the elements inside the sample. The sintering of ZrO_2-Y_2O_3 ceramics using SPS has been studied by several authors such as Dvilis et al. [38], Fregeac et al. [39], Bernard-Granger et al. [40], or Polla et al [41]. Different properties have been investigated after spark plasma sintering, such as optical transmission, electrical conductivity or mechanical properties (hardness, flexural strength, Young modulus). Also, their works clarified the link between the sintering temperature and the resulting microstructure and densification rate. For example, Dvilis et al. [38] studied the effect of the sintering temperature on the transparency of ZrO_2-$10Y_2O_3$ ceramics. As the transparency properties strongly depend on the microstructure and more particularly the grain size and porosity, the control of the evolution of the grain size with the sintering temperature has been enhanced. Also, a study in the field of nuclear energy presents the densification of yttria-stabilised hafnia using SPS, but with low yttria content (8.65 wt% of Y_2O_3) [42]. With this doping rate and considering their protocol before sintering, the authors have succeeded in obtaining almost dense pellets (> 90 % of the theoretical density) with a crack free and homogeneous microstructure. Few works also studied the formation of $RE_2Hf_2O_7$ phases, and for some of them including $Y_2Hf_2O_7$, but the samples are not elaborated using SPS sintering [19,43,44]. Finally, Wang et al. [45] reviewed the work done about the development of $A_2B_2O_7$ (including $Y_2Hf_2O_7$) materials using different elaboration processes for applications which require transparent ceramics. However, in their review, $Y_2Hf_2O_7$ ceramics are not sintered using SPS.

In this work, the influence of the nature of the stabiliser as well as its added amount has been studied using Spark Plasma Sintering (SPS). Thus, the objective of this study is on the one hand to investigate the possibility to use the SPS, instead of the standard natural sintering technique, for the sintering of HfO_2-Y_2O_3 ceramics stabilised with high yttria contents (33 mol. %, 40 mol. % and 50 mol. %), and on the other hand, to optimise the process parameters to obtain materials with the desired characteristics. In order to find the most appropriate sintering conditions, a systematic and iterative work has been performed to investigate the impact of the sintering temperature and the amount of Y_2O_3 content on both the crystallographic structure, as well as the chemical and microstructural homogeneity of the material.

2. Experimental procedure

2.1. Raw materials and sample manufacturing

A four-step manufacturing process is adopted to obtain dense pellets (39 mm in diameter, about 2 mm thick) of HfO_2, stabilised with different amounts of Y_2O_3, 33 mol. %, 40 mol. % and 50 mol. %. The manufacturing process is divided into the following phases: preparation of the mixture, pre-synthesis phase, SPS sintering and annealing treatment.

The protocol used for the first step of the manufacturing (preparation of the mixture) is identical to our previous study [1]. Thus, the two precursors, HfO_2 (purity 99.9 %, D_{50} < 1µm) and Y_2O_3 (purity 99.99 %, $0.5<D_{50}<1$ µm) are dried at 120 °C for at least 12 h and weighted to obtain the desired molar rates and ball-milled during 4 h into ethanol with zirconia media. Then, ethanol is extracted using a rotary evaporator and the resulting powder mixtures are screened through a 50 µm sieve to break weak agglomerates formed during the drying. The median diameter d_{50} of the raw powders are measured with a laser granulometer and are found to be 0.175 µm and 0.656 µm, respectively for HfO_2 and Y_2O_3. For the composition with 33 mol. % of Y_2O_3 a commercial mixture of powders is also considered in this study. Materials are named xYSHf with x the Y_2O_3 mol. % in the composition.

The second step is the pre-synthesis phase, where the powder mixtures are heat treated at 1550 °C for 2 h under air in a super Kanthal furnace. The aim of this step is to ensure the initiation of the formation of the desired cubic phase before the SPS sintering step, thus avoiding as much as possible reactive sintering in the SPS. The temperature of this thermal treatment (1550 °C) is too low to obtain a pure cubic phase powder. However, an increase of this temperature would have led to a partial sintering of the powder, which is not desired at this step. After this thermal treatment, weak agglomerates are broken in an agate mortar. At that point, it should be mentioned that the particle size distribution measured on the two 33YSHf powders is different (values summarised in Table 1 and Figure 1). Indeed, the median diameters are similar for both powders. However, the commercial powder exhibits a monomodal distribution while the powder from the laboratory is bimodal. This last point may be explained by the difference of initial particle size between the precursors of yttria and hafnia in the laboratory mixture. In addition, the span, which describes the particle size distribution, can be calculated from these results with the following formula:

$$\text{Span} = \frac{(d_{90} - d_{10})}{d_{50}} \quad (1)$$

where d_{90}, d_{50} and d_{10} are the diameters of the particles for which 90 vol. %, 50 vol. % and 10 vol. % of the particles are already counted.

The higher the value of the span, the more the particle size distribution is large. Generally, a span value close to 1 is correlated with a narrow particle size distribution. Here, the value of the span is almost identical for the two mixtures and relatively low, which reveals, in both cases, a good homogeneity in the particle size distribution.

Table 1: Characteristics of the 33YSHf powder mixtures used in the study (* measured with a laser granulometer).

Composition	Denomination	Supplier	D_{50} (µm) *	Span
Laboratory mixture HfO_2 + 33 mol% Y_2O_3	33YSHf (laboratory)	American Elements	2.56	3.13
Commercial mixture HfO_2 + 33 mol% Y_2O_3	33YSHf (CP)	Marion Technology	2.84	3.03

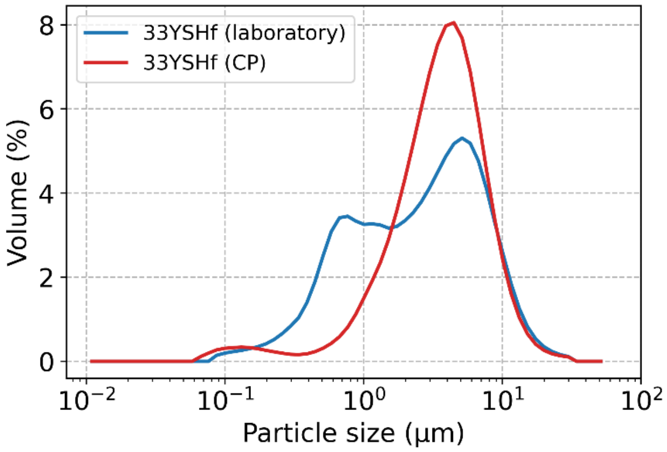

Figure 1: Particle size distribution of the 33YSHf commercial and laboratory powder mixtures.

The third manufacturing step is the sintering by SPS. A graphite die (Figure 2 (a)), with an internal diameter of 40 mm, is used to sinter about 20 g of powder (depending on the density of the mixture and the targeted thickness). To ensure a correct current transmission through the different parts of the mould, Papyex® sheets are settled between the die and the powder mixture.

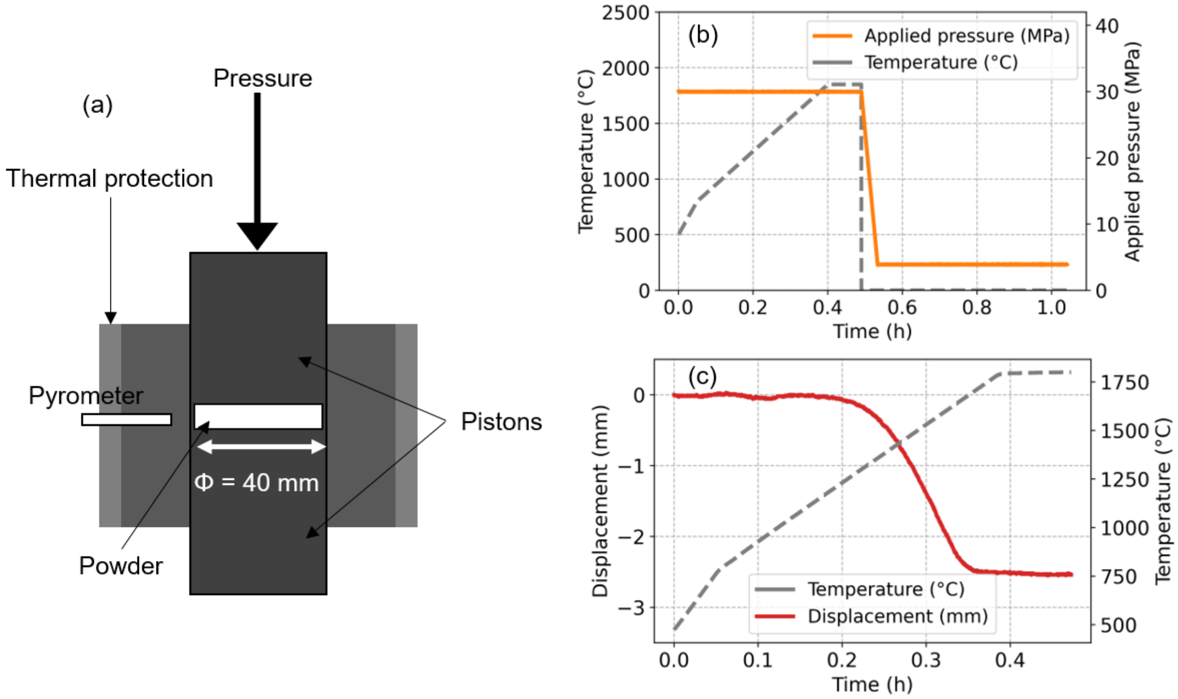

Figure 2: (a) Schematic view of the graphite die, (b) a typical sintering cycle and (c) a representative displacement curve of the sample 50YSHf - 1800 °C, versus time as a function of the temperature (measured by a pyrometer).

To assure the reproducibility of the experiments, the initial compaction rate of the green compact must be the same before the sintering. Indeed, the final shrinkage rate depends on the initial compaction rate. Thus, the powder mixture introduced into the graphite die is uniaxially pressed at ambient temperature. After that, the die is settled in the SPS chamber to begin the sintering process. A representative sintering cycle is shown in Figure 2 (b). Fixed elaboration parameters are the heating rate (100 °C/min until 800 °C and 50 °C/min until the final temperature), the uniaxial pressure (30 MPa), the atmosphere (vacuum up to 800 °C and argon (Ar) sweep until final temperature) and the sintering dwell-time (5 min). Above 800 °C, Ar is introduced into the chamber to limit the formation of oxygen vacancies. Since the objective of this study is to investigate the influence of the sintering temperature on the crystalline structure as well as the chemical and microstructural homogeneity of the materials, the only elaboration parameter varying is the sintering temperature (between 1600 °C and 1850 °C). The investigated sintering temperatures for each composition are gathered in Table 2. At the beginning of the cycle, and below 300 °C, the heating is controlled by a current ramp and beyond, in the 300-2500 °C range, the temperature is monitored by a lateral pyrometer.

Table 2: Compositions of the studied samples and the respective sintering parameters.

Composition of the sample	**Reference**	**Provider**	**Sintering temperature (°C)**					
			1600	**1650**	**1700**	**1750**	**1800**	**1850**
HfO_2 + 33 mol% Y_2O_3	**33YSHf (laboratory)**	**Laboratory mixture**	**x**			**x**		
	33YSHf (CP)	**Commercial Mixture**		**x**				**x**
HfO_2 + 40 mol% Y_2O_3	**40YSHf**	**Laboratory mixture**		**x**	**x**		**x**	**x**
HfO_2 + 50 mol% Y_2O_3	**50YSHf**	**Laboratory mixture**		**x**	**x**		**x**	**x**

At the end of the cycle, the sintering shrinkage is completed, which denotes the full densification of the pellets. This can be confirmed by the plateau visible at 1750 °C on the displacement curve (Figure 2 (c)).

The fourth and final step of the manufacturing process is the annealing treatment under air at 900 °C during 10 h in order to re-oxidise the samples and eliminate the carbon contamination, due to the graphite die that occurs during the sintering at high temperatures. The annealing conditions have been chosen considering our previous studies on similar or same compositions densified by the natural sintering route [1,2].

2.2. Sample characterisations

After samples elaboration, the cross-section surface and the top surface of the pellets are mechanically grinded with SiC papers and polished with diamond suspensions down to ¼ µm.

The crystal structure and phase composition are studied by X-ray diffraction (XRD). Diffraction patterns are collected using an Empyrean PANalytical X-ray diffractometer equipped with a Cu anode and a linear X'Celerator detector, set in the $\theta - \theta$ Bragg-Bretano geometry. The machine operates at 45 kV and 40 mA using a step size of 0.016° and 30s counting time per step, while the patterns are recorded from 10° to 110°. Furthermore, phase identification and profile fitting, using the full pattern Pawley method, are carried out with the HighScore Plus 5.1 software. Peak profiles are modelled using a pseudo-Voigt peak shape with a split width and shape asymmetry type, while the peak width (FWHM) is described using the Caglioti function [46]. A 7-term Chebyshev type I background function is used and the refined parameters are the specimen displacement, the lattice parameters, the Caglioti U, V and W variables and the peak shape 1, 2 and 3.

The crystalline phases, identified with the aid of ICDD PDF-4+ 2022 database and considered in the Pawley analysis as well, are: the $Y_2Hf_2O_7$ (PDF #01-085-7578), the $Y_{1.69}Hf_{0.31}O_{3.155}$ (PDF #04-024-8877), the HfO_2 (PDF #00-053-0560) and the Y_2O_3 (PDF #00-041-1105). A quantitative phase analysis is also performed using the so-called "Direct Derivation (DD)" method proposed by Toraya in 2018 [47] , which is an option in the HighScore Plus 5.1 software.

The microstructural and chemical characterisation is performed using a Tescan Mira3 Schottky FEG-SEM equipped with an EDAX Octan Elite EDS (Energy Dispersive Spectroscopy) and an EDAX Velocity EBSD (Electron Back Scattered Diffraction system) detector. The SEM images are acquired at 15 kV with beam current around 5 nA.

The carbon content inside the material is measured with a high precision elemental analyser Inductar CS. This analyser is equipped with an induction furnace and an infrared detector, which detects the CO_2 formed during the melting of the sample under oxygen flux. As the melting temperature of hafnia is very high, a binary additive (SnW) is added with the sample into the furnace to lower its melting temperature.

3. Experimental results

3.1. Microstructure and chemical composition

XRD, SEM, EDS and EBSD analyses were carried out to provide information about the influence of the amount of Y_2O_3 and the sintering temperature on the chemistry and the microstructure. With appropriate SPS sintering conditions, pellets have been successfully densified. Indeed, as residual porosity (measured with the Archimedes' method) is below 1 %, the materials are considered as fully dense.

X-ray diffraction analysis were carried out both on powders, after the pre-synthesis step (1550 °C - 2 h), and on polished surfaces of sintered samples by SPS. A representative example is presented in Figure 3(a), where the raw data of sample 40YSHf after the pre-synthesis step and after the SPS sintering step (at 1700 °C) are superimposed.

On Figure 3(b), three peaks are detectable for the black curve, corresponding to the powder before sintering. After identification, they were respectively associated to the two precursors which are Y_2O_3 and HfO_2 and to the final foreseen product $Y_2Hf_2O_7$. Regarding the red curve corresponding to the sample after sintering, the specific peak of $Y_2Hf_2O_7$ is observable with a shoulder on the low angles, which is associated to another intermediate phase $Y_{1.69}Hf_{0.31}O_{3.155}$. For sintered materials, XRD analyses revealed that pure hafnia and yttria are no more detected, or, for some samples, only in very small proportions. However, the presence of an intermediate Y-Hf-O phase is detectable and corresponds to the hump observed at the base of the major peak.

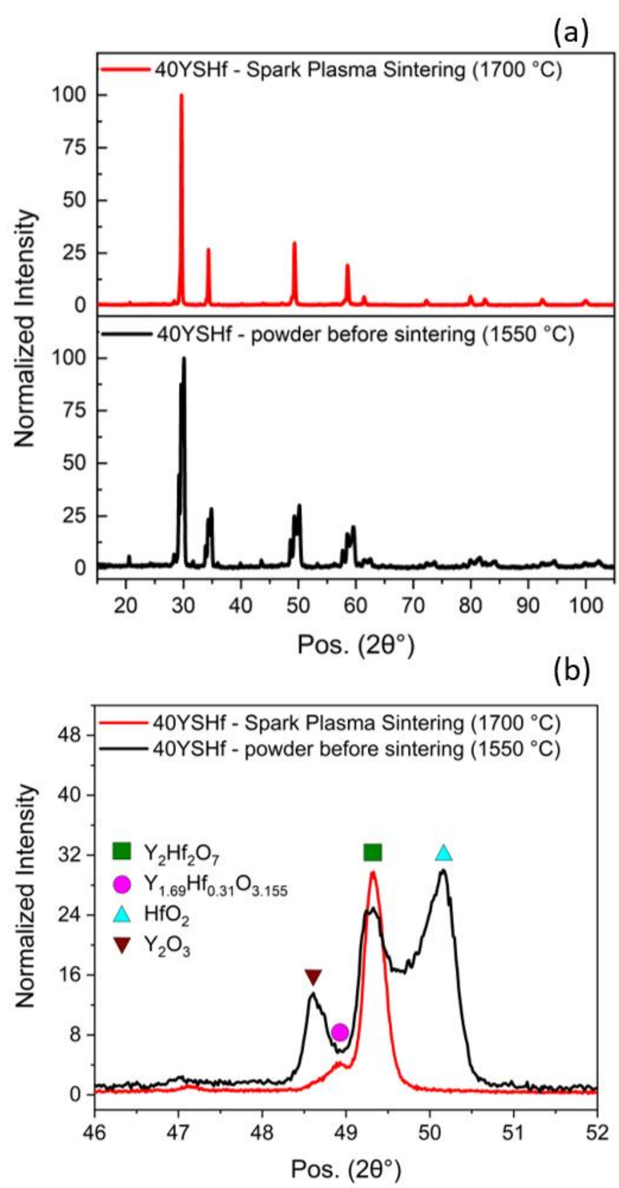

Figure 3: (a) X-ray diffraction patterns of a 40YSHf sample after SPS sintering (1700 °C) and of a 40YSHf powder mixture after the pre synthesis heat treatment (1550 °C) before sintering and (b) zoom on the X-ray diffraction patterns ($46<\Theta<52$) and phase identification of the samples from (a).

The X-ray diffraction patterns of the 40YSHf sample sintered at 1700 °C is presented in Figure 4 with a zoomed image inside. The data are recorded for 2Θ from 10 to 110 ° but are presented from 20 to 70 ° to provide a better visualisation. The solid lines correspond to the experimental (red) and calculated (black) data and the blue solid line at the bottom is the difference between the calculated and observed profile (Rwp = weighted profile residue). The Rwp is close to 5, which attests the accuracy of the calculated fit. The different identified phases are quantified and are represented in the zoomed part by the green ($Y_2Hf_2O_7$), pink ($Y_{1.69}Hf_{0.31}O_{3.155}$), light blue ($HfO_2$) and brown ($Y_2O_3$) lines.

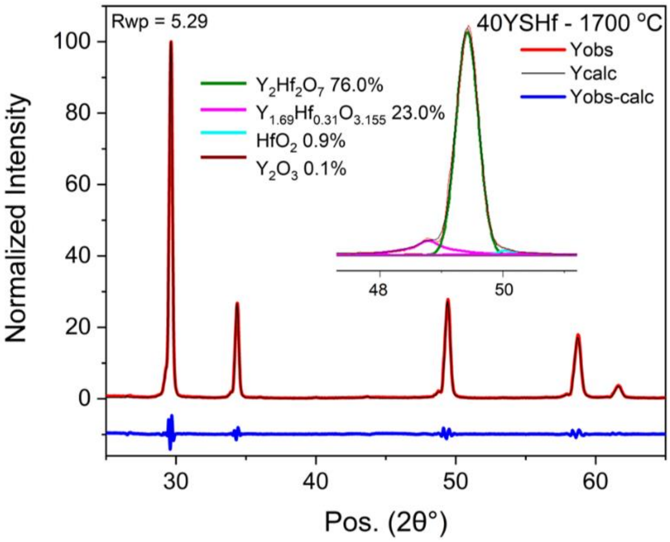

Figure 4: X-ray diffraction patterns of a 40YSHf sample sintered by SPS at 1700 °C and corresponding Pawley refinement with quantification of the phases obtained with the Direct Derivative Quant Method.

The sample sintered by SPS technique presents 23.0 wt% of yttria-rich phases (mostly constituted of the intermediate phase $Y_{1.69}Hf_{0.31}O_{3.155}$). The presence of precursors is still detectable too but in very low content (< 1 wt%). The presence of the intermediate phase in significant proportion seems to be related to the sintering process itself. In all cases, $Y_{1.69}Hf_{0.31}O_{3.155}$ and Y_2O_3 phases crystallise in the same space group Ia-3 and are chemically very close.

Figure 5 shows the X-ray diffraction patterns of different spark plasma sintered samples. The influence of the sintering temperature and the amount of Y_2O_3 on the crystallinity of the structure is clearly visible. As a result, the more the amount of Y_2O_3 and the sintering temperature are high, the more the structure is constituted of bigger crystallites. Moreover, the hump observed for all the samples close to the major peak, which corresponds to the presence of the intermediate phase, is less visible for lower amounts of Y_2O_3 (Figure 5 (a)) and for higher sintering temperatures (Figure 5 (b)). This point, which will be quantified below means that the formation of the cubic phase $Y_2Hf_2O_7$ is favoured with the increase in temperature and for 40 mol. % of Y_2O_3 compared to 50 mol. %. This observation is correlated with the simultaneous disappearing of the intermediate phase ($Y_{1.69}Hf_{0.31}O_{3.155}$) and initial phases ($Y_2O_3$ and HfO_2). Moreover, a peak shift to lower angles is clearly visible with the increase in the yttria amount for a constant sintering temperature or with the increase in temperature for a constant amount of yttria. This shift is related to the evolution of the chemical composition associated to the stoichiometry of the fluorite phase.

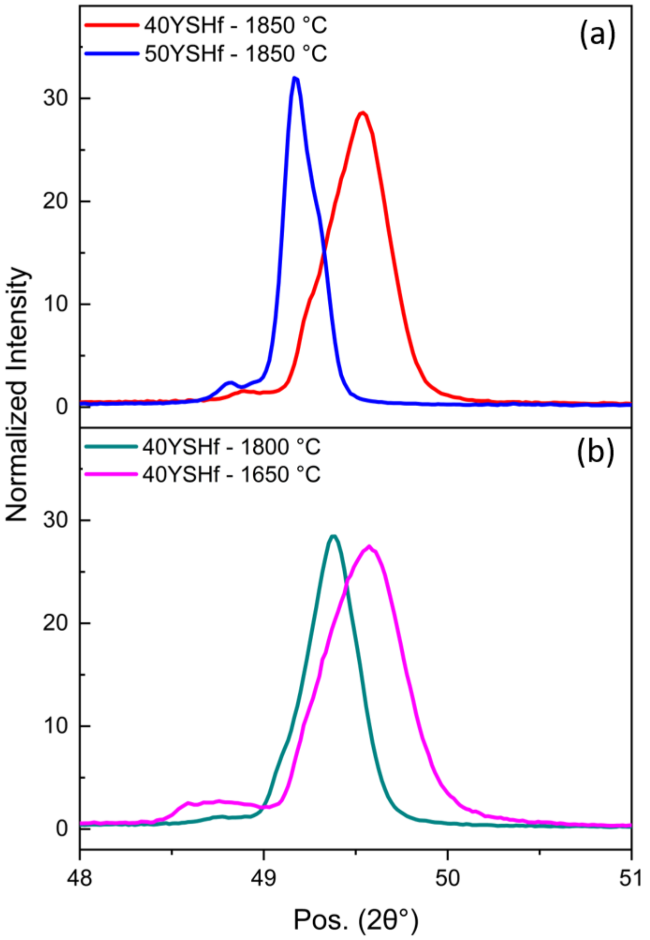

Figure 5: X-ray diffraction patterns of (a) 40YSHf and 50YSHf samples sintered at 1850 °C and (b) 40YSHf samples sintered at 1650 °C and 1800 °C.

A deeper study has been performed to analyse the influence of sintering temperature and amount of yttria in hafnia on the values of the lattice parameter of the main $Y_2Hf_2O_7$ phase. Moreover, the proportions of intermediate phase and precursors (initial phases) have been quantified for each sample. The precursors are present in smaller amounts compared to the intermediate phase. Actually, the $Y_{1.69}Hf_{0.31}O_{3.155}$ phase is an intermediate solid solution composition generated during the formation of the fluorite phase.

Results regarding the lattice parameter for 33YSHf, 40YSHf and 50YSHf are presented in the Figure 6(a). Two main observations can be deduced from these outcomes. Firstly, the increase in temperature leads to an increase in the lattice parameter. However, it seems that a slight decrease could be recorded for the highest temperatures. Secondly, the higher the amount of Y_2O_3, the higher the lattice parameter. Additionally, the commercial mixture (33YSHf (CP) for samples elaborated at 1650 °C and 1850 °C) seems to allow a better formation of the cubic phase as the lattice parameter is close to the theoretical lattice parameter of the cubic $Y_2Hf_2O_7$ phase determined in the JCPDS file, which is 5.196 Å. This fact may be explained by an optimised preparation of the commercial mixture, which can induce a better chemical homogeneity of the powder mixture. This last point can generate a difference in the diffusion processes as a more homogeneous mixture of the raw powders provides a better inter diffusion between the compounds and thus a better formation of the desired phase. The better chemical homogeneity of the commercial powder is clearly visible in the Figure 1 as the particle size distribution is monomodal whereas the powder from the laboratory is bimodal. Moreover, for higher amounts of Y_2O_3 and higher sintering temperatures a peak shift to lower angles is observable in Figure 5. This peak shift implies an increase of the lattice parameter (Figure 6(a)) .

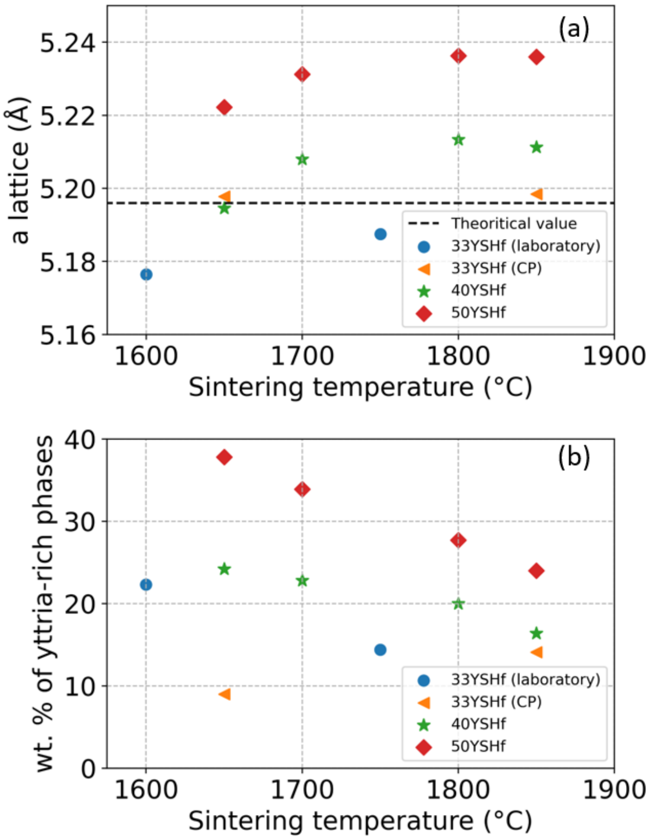

Figure 6: (a) Evolution of the lattice parameter of the cubic $Y_2Hf_2O_7$ phase with the sintering temperature for yttria containing compositions (CP indicates the commercial powder) and (b) evolution of the proportion of the yttria rich phases ($Y_{1.69}Hf_{0.31}O_{3.155}$ and Y_2O_3) with the increase in sintering temperature for different amounts of Y_2O_3 in HfO_2.

The quantification of the phases with the Direct Derivation Method confirmed that the proportion of the $Y_{1.69}Hf_{0.31}O_{3.155}$ phase decreases with the increase in temperature and with the diminution of the amount of Y_2O_3 (Figure 6(b)). The variation between the amount of principal ($Y_2Hf_2O_7$) and intermediate phases explains the increase of the lattice parameter with the temperature as the formation of the main phase is favoured.

As it has been demonstrated with XRD analysis, microstructural analysis (SEM-BSE) confirmed that chemical inhomogeneities are detected. Additionally, the samples present grain size heterogeneities. Indeed, Figure 7(a) displays SEM images of 40YSHf samples sintered between 1650 °C and 1850 °C. It is clearly visible that the proportion of black spots, which represent the intermediate phase and Y_2O_3, decreases with the temperature increase. Moreover, the more the sintering temperature is high, the more microcracks (mostly intergranular) appear in the microstructure at 1800 °C and 1850 °C. This is a witness of the damage of the sample.

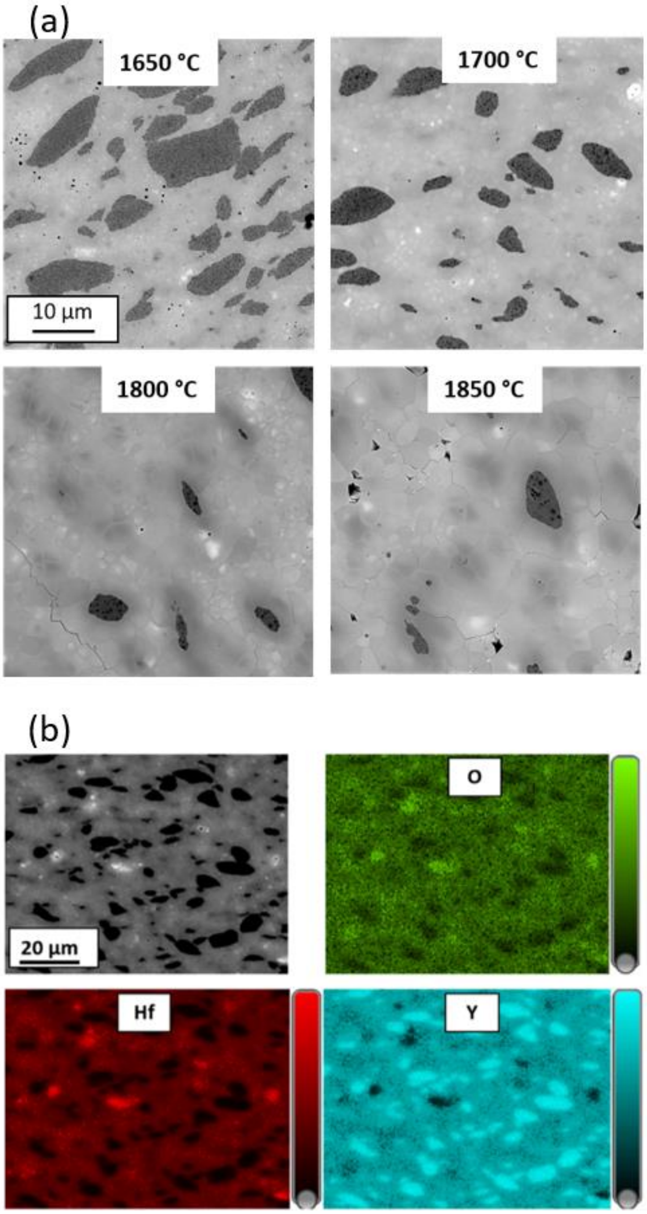

Figure 7: (a) SEM (BSE) images of 40YSHf samples sintered using SPS as a function of the sintering temperature: evolution of the proportion of yttria-rich phases and (b) EDS analysis of the 40YSHf sample sintered at 1700 °C associated to the SEM corresponding image.

Those observations have been coupled to chemical analysis with an EDS system on some zones of interest. A representative case is shown in Figure 7(b) for the 40YSHf sample. The elemental EDS cartography allows us to conclude that fine grains located in dark areas corresponds to Y_2O_3 rich regions.

Moreover, BSE images reveal the presence of four chemical composition nuances (Figure 8 (a)), which can be correlated to the different phases detected through XRD analyses. Dark spots (zone 1) are Y_2O_3-rich areas containing pure Y_2O_3 inside them whereas white spots (zone 4) are HfO_2-rich regions (Figure 8 (b)). In the same figure two intermediate nuances are also observable (zones 2 and 3), which could correspond to different concentrations of the elements in the Y-Hf-O system. As the precise stoichiometry of this phase is not easily determinable, it is associated to $Y_{1.69}Hf_{0.31}O_{3.155}$ using XRD.

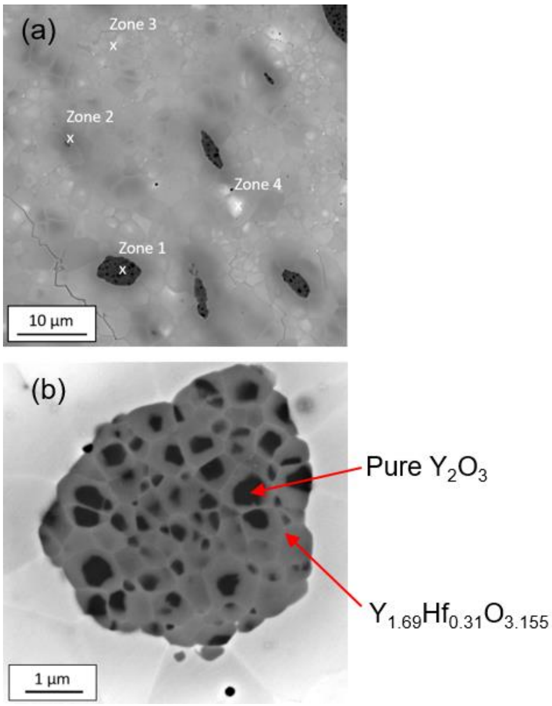

Figure 8: SEM-BSE observations of the 33YSHf sample sintered using SPS at 1750 °C: (a) observation of four contrasted zones, corresponding to different chemical compositions and (b) zoom on the zone 1: black spots inside the dark nuance corresponding to pure Y_2O_3.

To complete and confirm the previous results, EBSD analyses were carried out to allow the precise determination of the grain size distribution on each sample and thus link the grain size to the sintering temperature. For 33YSHf samples, only one population of grain size is observed. For 40YSHf and 50YSHf samples, two populations of grain size are present in each sample, unless for 40YSHf sintered at 1850 °C. Then, two analyses at different scales have been done to determine both the ratio between the two populations of grains and the average grain size of each population. For the smaller grain size, several spots of small grains have been isolated in one EBSD map to optimise the calculation time. Figure 9 presents an example of an EBSD image of a 40YSHf sintered sample. In Figure 9 (a), the analysed coloured zones are related to the $Y_2Hf_2O_7$ phase whereas the black areas correspond to Y_2O_3-rich zones presented in Figure 9 (b). These areas, which are constituted of finer grains, are composed of $Y_{1.69}Hf_{0.31}O_{3.155}$ and Y_2O_3.

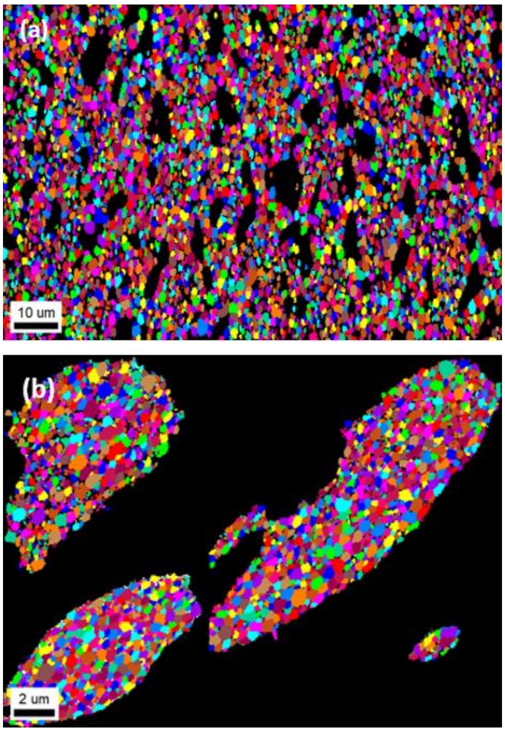

Figure 9: Representative EBSD analysis (grain maps) of a sintered sample (40YSHf, 1650 °C) at two different scales (a) HfO_2-rich zones and (b) zoom on dark areas of an Y_2O_3-rich zone.

From these EBSD analyses, grain size has been determined for all the samples and the results are reported in the Figure 10. It can be deduced that an increase in sintering temperature implies grain growth. However, with the SPS sintering technique, this grain growth is limited to a few µm. Indeed, in all cases, the final grain size of the coarse grain population is below 10 µm. This demonstrates that the SPS process is successful in limiting the undesired grain growth. Moreover, this study allows quantifying the evolution of grain size for both fine and coarse grain populations.

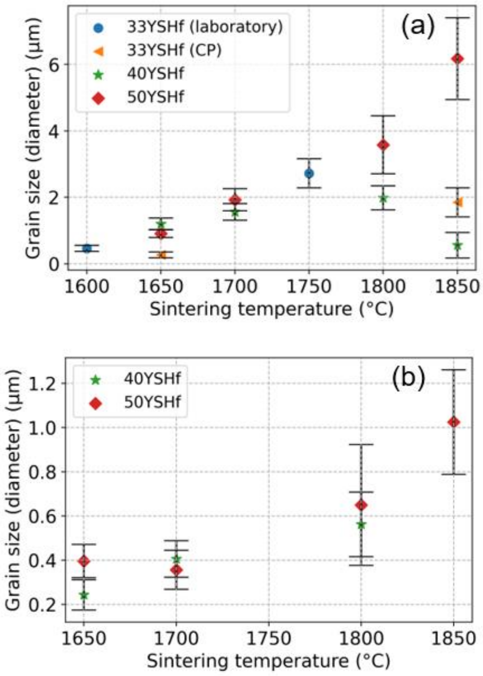

Figure 10: Grain size evolution with sintering temperature, from the EBSD analysis for (a) the population of the coarsest grain size ($Y_2Hf_2O_7$ phase) and (b) the population of the smallest grain size (Y_2O_3-rich phases).

Moreover, for the 50YSHf composition, the evolution of the coarsest grain size, which correspond to the $Y_2Hf_2O_7$ phase is rather linear whereas for the 40YSHf, the grain size decreases above 1800 °C. This last point can be explained by the fact that only one population of grain size has been detected for this composition at this temperature (Figure 11), which is strongly correlated with the lower amount of yttria-rich areas in the 40YSHf. Indeed, compared to the 50YSHf sample sintered at the same temperature, the 40YSHf is chemically more homogenous. Considering this point, the decrease in grain size may be explained by chemical homogenisation effects as the yttria-rich phases diffuse through the matrix part and contribute to reduce the overall size of this part, which becomes chemically more and more homogeneous.

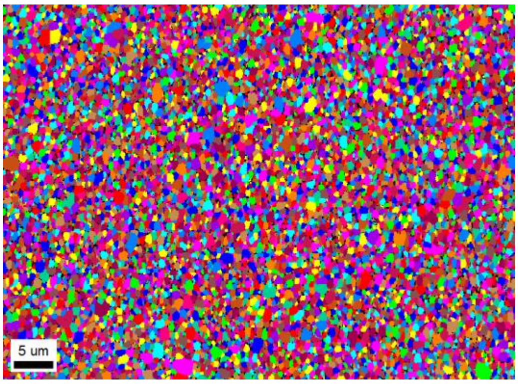

Figure 11 : EBSD grain map of the 40YSHf sample sintered at 1850 °C, showing the presence of only one grain size population.

3.2. Carbon contamination of samples sintered by SPS

For all the samples densified by SPS technology, the use of a graphite die during the sintering process at very high temperatures implies carbon contamination. This is visible on the monolithic materials obtained after sintering whose colour is mostly very dark. So, the influence of the sintering temperature on the carbon contamination has been also studied and the results are gathered in Figure 12. In order to quantify the amount of carbon absorbed during the process, a gas analyser based on infrared absorption has been used on sintered samples before the annealing post treatment. Moreover, to try to determine the critical temperature implying carbon contamination, a sample has been also sintered by SPS at lower temperature (1550 °C).

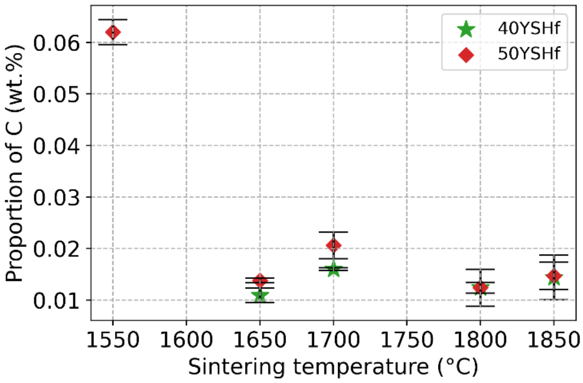

Figure 12 : Quantification of the proportion of absorbed carbon during the SPS process as a function of the sintering temperature.

Actually, the colour of the sample does not seem directly related to the quantity of carbon in the sample as the sample sintered at 1550°C is fully white and exhibits the highest amount of C. However, it could be explained by the mechanism of electrochemical reduction discussed in the following part and the physical stabilisation of carbon (gaseous form or solution). Moreover, it seems that there is no variation of absorption between the different rates of yttria in hafnia.

4. Discussion

4.1. Microstructure and chemical composition

This study aims to understand the impact of sintering temperature and amount of Y_2O_3 on densification, chemistry, microstructure and crystallographic structure of hafnia-based ceramics.

All the studied samples are considered to be fully dense. Indeed, figure 7(a) demonstrates that full densification is achieved for a sintering temperature of 1700 °C and does not evolve up to 1850 °C. However, the sample sintered at 1550 °C (50YSHf) is not dense (23 % of open porosity and 1 % of closed porosity) indicating that densification mechanisms still occur for temperatures between 1550 and 1700 °C. Li et al. [48] studied the sintering of nano-sized ZrO_2-$3Y_2O_3$ powder mixtures ceramics and in particular the link between the sintering temperature and the relative density. They highlighted the fact that above 1400 °C, ceramic samples are dense (99 %) having nano-sized particles (6-8 nm) and that a further increase in sintering temperature does not lead to an increase in densification rate. Even if the composition is different to those investigated in this study, the same tendency is observed in the present work. As hafnia is a bit more refractory than zirconia and the mixtures have larger particle sizes, it is not surprising that the densification happens at higher temperatures compared to zirconia. Additionally, the pressure applied during sintering is different in the study of Li et al. (40 MPa) compared to the present case (30 MPa), which has an impact on the densification and the final particle size.

The fact that the increase of the sintering temperature, in the case of yttria-stabilised hafnia, leads to a grain growth, has already been observed for zirconia based compositions obtained by different processes including SPS, but for lower amounts of stabiliser. For instance, Dvilis et al. [38] studied the influence of the sintering temperature on the grain size of HfO_2-ZrO_2 ceramics elaborated by SPS and found that an increase of the sintering temperature from 1200 to 1400 °C leads to an increase of the grain size from 307 nm to 1.766 µm. This is linked to the fact that at 1200 °C, the sintering process is not complete resulting to a grain size corresponding to the initial powder size. In the present work, the grain size also increases with the sintering temperature and remains in the micrometric range. However, the densification occurs at a higher temperature compared to their study, which is most probably related to the larger size of the raw powders in our study. The increase of the grain size with the sintering temperature could also be related to the higher crystallinity of the structure, as revealed by XRD analyses in our study. Indeed, at the end of the sintering process, for high temperatures, sintering is governed by grain growth mechanisms, as the elimination of open porosities occurs at lower temperatures during the intermediate stage of sintering, as explained by Flaureau et al. [49]. Moradkhani et al. [50] suggested that for their nanoSiC-Al_2O_3 composites, the volume fraction of SiC nanoparticles is correlated to the grain size. The addition of SiC nanoparticles located at the grain boundaries limits the grain growth in the matrix but also the sintering, thus having an impact on the final density. Even if a comparison can be done between Moradkhani's work and the present study, this example should be considered with caution, as there is no solid solution formation with SiC-Al_2O_3 compositions. They mentioned the Zener's model which demonstrates that the presence of a secondary phase implies a limitation of the grain growth for the matrix part. In our case, the matrix may be constituted of $Y_2Hf_2O_7$ and the secondary phase composed of yttria-rich phases ($Y_{1.69}Hf_{0.31}O_{3.155}$ and Y_2O_3). The Zener's model is described by the following equation:

$$G = \frac{4r}{3f} \tag{2}$$

where G is the grain size of the matrix (µm), r the grain size (radius) of the secondary phase (µm) and f the volume fraction of the secondary phases (%). Figure 13 represents the comparison between the experimental determination of the matrix grain size and the matrix grain size obtained by the Zener's model. To use the model, the volume fraction of the secondary phases has been determined using XRD analyses whereas the grain size of the secondary phases has been obtained from EBSD grain maps. As the XRD data are initially in wt%, an assumption has been done concerning the secondary phases to convert them to volume fractions: thus, the density of the secondary phases has been considered equal to the density of $Y_{1.69}Hf_{0.31}O_{3.155}$ as it is the predominant phase inside the yttria-rich areas.

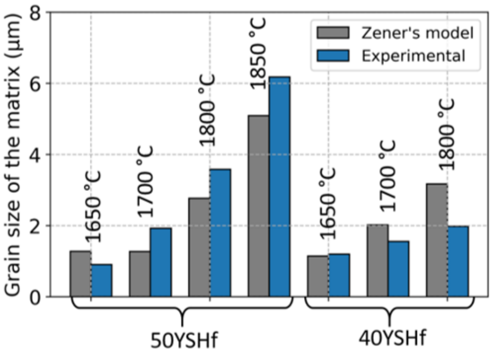

Figure 13: Comparison between the grain size of the matrix for 40YSHf and 50YSHf samples using the Zener's model (based on the experimental size of the secondary phase obtained by EBSD analysis and the experimental volume fraction of the phases determined from XRD analysis) and the experimental size of the matrix (obtained by EBSD analysis).

Considering, the uncertainty in the determination of the volume fraction of the secondary phases and that an error is done on the density of these secondary phases, the experimental and calculated values are in good agreement.

Thus, both the sintering temperature and the presence of the intermediate phase or precursors could affect the final grain size of the samples manufactured by SPS. The intermediate phase remaining during the solid solution formation acts as a grain growth inhibitor in this case.

The volume fraction of the yttria-rich phases evolves with the sintering temperature but also with the amount of Y_2O_3. Indeed, stoichiometric calculations show that 33 mol. % of Y_2O_3 leads to complete $Y_2Hf_2O_7$ formation. Higher amounts of Y_2O_3 lead to the formation of $Y_2Hf_2O_7$ plus some residual Y_2O_3, or at least, to yttria rich Y-Hf-O phases.

The summary of theoretical results compared with experimental data is presented in Table 3.

Table 3: Experimental/theoretical comparison between the proportion of the main phase and yttria-rich phases for the different compositions (in wt%).

	Theoretical values		SPS sintering (1850 °C)	
	$Y_2Hf_2O_7$	$Y_{1.69}Hf_{0.31}O_{3.155}$ and Y_2O_3	$Y_2Hf_2O_7$	$Y_{1.69}Hf_{0.31}O_{3.155}$ and Y_2O_3
33YSHf	100	0	86	14
40YSHf	90	10	84	16
50YSHf	74	26	76	24

So, the more the amount of Y_2O_3, the more the quantity of yttria-rich phases. This is in good agreement with the XRD results presented in the Figure 6(b). For the material with 50 mol. % of Y_2O_3 sintered by SPS, the proportion of these phases is 24 wt%, which is very close to the theoretical value (26 wt%); for 40 mol. % this experimental proportion is 16 wt%, which is 6 wt% higher than theoretical forecasts. Also, for 33 mol. % of Y_2O_3, the experimental quantifications associated with SEM analysis reveals the presence of yttria-rich phases (of about 14 wt%) even if the theoretical calculations indicate the formation of the main phase at 100 wt%. This deviation may be attributed to, both the process itself and the nature of the powders. Indeed, using the SPS technique, dwell time sintering was fixed to 5 min and heating rates were 100 °C/min and 50 °C/min. These conditions, which are rather different from natural sintering [1] reduce the time useful for reaction and diffusion mechanisms between the different species of the composition, which limit the formation of the main fluorite phase. As diffusion mechanisms imply in the solid solution formation are time and temperature dependant, this explains the differences between spark plasma and naturally sintered samples.

Thus, diffusion processes, responsible for the complete formation of the desired phase and the reduction of heterogeneities, does not have time to fully occur during SPS processes. On the other hand, the short dwell time, associated with the uniaxial pressure applied during the process, provides small grain size and very high density. As a result, chemical homogeneity is better using natural sintering than using SPS for the same composition [1].

Additionally, another explanation for the presence of yttria-rich phases is that diffusion rate of Y^{3+} ions is different from diffusion rate of Hf^{4+} ions in the final solid solution $Y_2Hf_2O_7$. This difference leads to possible micropores in place of the initial Y^{3+} location, which may limit sintering as they become closed pores remaining after elaboration. This “Kirkendall effect”, has previously been observed in the literature, for HfO_2-Y_2O_3 compositions [51] and for 7YSZ-Gd_2O_3 composites [52]. In consequence, for low sintering temperatures, the increase in the amount of Y_2O_3 could limit the shrinkage and thus slowing down the diffusion mechanisms between the species and finally, leading to a low amount of the foreseen $Y_2Hf_2O_7$ phase.

Finally, as revealed by the XRD measurements, the lattice constant of the sintered YSHf increases with increasing the amount of Y_2O_3 (Figure 6(a)). This phenomenon has already been observed in the literature for stabilised zirconia and in one of our previous study as well for stabilised hafnia [1,32,53–55]. This could be explained by the increase of the amount of rare earth oxide, in the matrix for which the ionic radius of the corresponding cation is larger than the one of Hf^{4+}. More specifically, the ionic radii of Hf^{4+} is 0.83 Å whereas the ionic radii of Y^{3+} is 1.02 Å. Thus, the higher the amount of Y^{3+} incorporated into the HfO_2 lattice, the higher the lattice expansion. Consequently, stoichiometric deviation from the perfect $Y_2Hf_2O_7$ composition is possible by increasing the Y_2O_3 amount.

4.2. Carbon contamination of samples sintered by SPS

Fully black pellets were obtained after SPS sintering above 1600 °C. This phenomenon is called the “blackening effect”. Actually, two mechanisms that are competing during the sintering process, are responsible for this effect: firstly, the reduction of the ceramic (as electrons are moving into new vacancy sites in the crystalline structure because the process is running under Ar atmosphere); secondly, the carburation of the ceramic at high temperatures. Moreover, some authors highlighted the fact that their ceramic specimens became electronically conductive during the sintering which means that electrons moved into the crystalline structure. This phenomenon can be explained by the dissociation of uncharged vacancies, according to the equation 3 [56] :

$$V_O^x = V_{O}^{\cdot} + e' = V_{O}^{\cdot\cdot} + 2e' \tag{3}$$

To re-oxidise the samples and eliminate the carbon contamination, samples were annealed at 900 °C during 10 h under air. The black colour mostly disappeared but few samples were not homogeneously oxidised. Indeed, this annealing process generates two types of damages, especially for samples sintered at the highest temperatures: (i) large pores and cracks appear, particularly on one face of the pellets and (ii) small intergranular pores are formed through all the thickness of the sample. Moreover, increasing the annealing temperature up to 1550 °C amplifies these phenomena as it can be seen on SEM examinations (Figure 14).

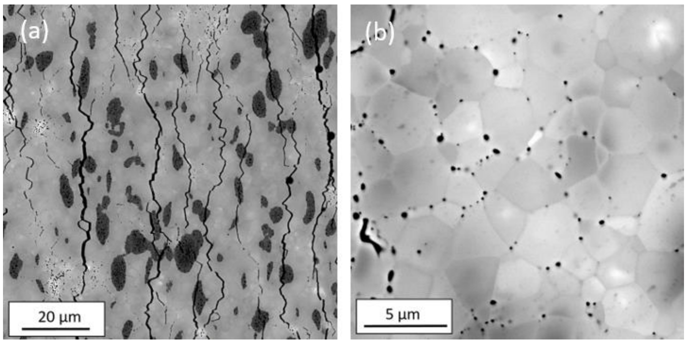

Figure 14 : SEM (BSE) observations of two re-oxidised samples after annealing treatment at 1550 °C under air (a) large cracks on one side of the 50YSHf sample sintered at 1700 °C and (b) small intergranular pores in the 40YSHf sample sintered at 1800 °C.

Thus, above a certain sintering temperature in the SPS process, the material is damaged. The first type of degradation, specifically observed close to one surface, could be related to the temperature gradient generated within the thickness of the material during the sintering. Indeed, due to a thermal gradient occurring during the sintering process itself and the high heating and cooling rates (as the ceramic powders are not electrically conductive), residual mechanical stresses are present in the samples after sintering. These residual stresses might relax during the annealing process, which can consequently generate cracks. Fattahi at al. [57] studied the impact of the sintering temperature on the properties of TiC-SiC_w composites. For samples sintered at 2000 °C they note a diminution of flexural strength and hardness compared to samples sintered at 1900 °C. Moreover, they observe the formation of extra pores at 2000 °C. Also, in our study, for very high sintering temperatures (between 1800 °C and 1850 °C), the lattice parameter does not seem to evolve anymore (Figure 6). Thus, Y_2O_3 has reached a maximum of solubility in $Y_2Hf_2O_7$. The diffusion mechanisms may be stopped because of the damage of the material and this can be correlated to a too high amount of C in the material.

The second type of damage is likely to be related to the carbon contamination. There is no evidence of the mechanism conducting to carbon contamination but some hypotheses suggest that gaseous carbon phases could be generated during heating. These carbon-based gases, mainly CO and CO_2, can be trapped into pores and, become closed pores with densification [37], and decompose into solid carbon and gases. Thus, during the annealing process, the solid carbon could become gaseous again. This may explain the formation of intergranular porosities as Morita et al. [37] find that carbon phases segregates along grain boundaries.

Moreover, this mechanism could justify the fact that even if white pellets were obtained at 1550 °C, the amount of carbon was higher than in the pellets sintered at higher temperatures. Indeed, the densification rate of white pellets is lower as it has been evaluated around 76 vol. % with the Archimedes' method, and is mostly constituted of open porosity (for 23 vol. %). So, for those samples, we can assume that the densification level is not high enough to allow the decomposition of gaseous carbon into solid phases, which are responsible for the black colour of the pellets. Thus, for sintering temperatures below 1600 °C, the high amount of carbon present in the samples is mainly due to gaseous phases trapped into closed pores (1 vol. % of closed porosity). Additionally, with the used technique, the detection of gaseous carbon is easier than the one of carbon in solution. Thus, we can say that the carburation of the compounds is present at temperatures higher than 1600 °C, even if the quantification of C in the materials is very difficult with simple techniques.

5. Conclusion

This work showed that SPS can be successfully used for the elaboration of HfO_2-Y_2O_3 materials allowing the quick manufacturing of dense pellets with fine microstructure.

1) It is a fast technique for the production of dense material at lower temperatures compared to natural sintering, which is important since the grain overgrowth can be avoided. As the pressing and sintering steps are executed at the same time, the number of manufacturing steps is reduced.
2) However, there are still few challenges that should be addressed and further investigated as it generates significant microstructural heterogeneities. The blackening effect due to oxygen vacancies formation and carbon contamination during the process induces damages (pores and cracks) in the samples during the annealing process. Optimising the manufacturing conditions by aiming to limit the reduction of the oxide, is part of our perspectives.
3) Furthermore, temperature as well as the amount of Y_2O_3 play a crucial role on the crystallographic, microstructural and chemical homogeneity of the sintered material. The increase in the sintering temperature leads to the formation of a monophasic material of the foreseen cubic phase $Y_2Hf_2O_7$, reducing significantly the proportion of secondary phases such as the yttria-rich phase. In addition, this implies an increase of lattice parameter, crystallinity of the structure and grain size. However, above 1800 °C, the amount of the cubic phase does not evolve anymore. So, the ideal sintering temperature should be below 1800 °C.
4) The increase of the amount of Y_2O_3, which may be favorable for a decrease of the ionic conductivity, generates the formation of a higher proportion of the additional intermediate phase and an increase of lattice parameter and grain size for the same sintering temperature. The impact of the presence of a high amount of intermediate phase on the final properties of the material is currently under investigation and will be presented in a forthcoming work.

In addition, further investigations on thermal and ionic conductivity will be held in another study to select the optimised ceramic composition for further use in the FGM field.

Acknowledgments

The authors acknowledge Denis Boivin (ONERA) for his advices and knowledge sharing in SEM imaging and Katia Dennis (ONERA) for her assistance with the sample preparation. This study was part-financed by CNES. ICB is supported by the EUR-EIPHI Graduate School (Grant No. 17-EURE-0002).

6. References

[1] L. Sévin, V. Razafindramanana, A. Julian-Jankowiak, J.-F. Justin, F. Mauvy, F. Rebillat, Effect of high-content Yttria on the thermal expansion behaviour and ionic conductivity of a stabilised cubic Hafnia, Journal of the European Ceramic Society. 40 (2020) 5859–5869. https://doi.org/10.1016/j.jeurceramsoc.2020.05.044.

[2] A. Julian-Jankowiak, L. Sévin, V. Razafindramanana, L. Audouard, J. Justin, P. Bertrand, C. Langlade, M. Garcia, Manufacturing and characterisations of hafnia-based materials for aerospace applications, (2022). https://doi.org/10.13009/EUCASS2022-6082.
[3] N.P. Padture, Advanced structural ceramics in aerospace propulsion, Nature Materials. 15 (2016) 804–809. https://doi.org/10.1038/nmat4687.
[4] D. Zhou, O. Guillon, R. Vaßen, Development of YSZ Thermal Barrier Coatings Using Axial Suspension Plasma Spraying, Coatings. 7 (2017) 120. https://doi.org/10.3390/coatings7080120.
[5] E. Bakan, R. Vaßen, Ceramic Top Coats of Plasma-Sprayed Thermal Barrier Coatings: Materials, Processes, and Properties, Journal of Thermal Spray Technology. 26 (2017) 992–1010. https://doi.org/10.1007/s11666-017-0597-7.
[6] R. Vaßen, M.O. Jarligo, T. Steinke, D.E. Mack, D. Stöver, Overview on advanced thermal barrier coatings, Surface and Coatings Technology. 205 (2010) 938–942. https://doi.org/10.1016/j.surfcoat.2010.08.151.
[7] K.P. Jonnalagadda, R. Eriksson, K. Yuan, X.-H. Li, X. Ji, Y. Yu, R.L. Peng, Comparison of damage evolution during thermal cycling in a high purity nano and a conventional thermal barrier coating, Surface and Coatings Technology. 332 (2017) 47–56. https://doi.org/10.1016/j.surfcoat.2017.09.069.
[8] C.G. Levi, Emerging materials and processes for thermal barrier systems, Current Opinion in Solid State and Materials Science. 8 (2004) 77–91. https://doi.org/10.1016/j.cossms.2004.03.009.
[9] R.A. Miller, G.W. Leissler, J.M. Jobe, Part I: Effect of Spray Parameters on the Performance of Several Lots of Partially Stabilized Zirconia-Yttria Powder, NASA Technical Paper 3295. (n.d.) 34.
[10] D.R. Clarke, S.R. Phillpot, Thermal barrier coating materials, Materials Today. 8 (2005) 22–29. https://doi.org/10.1016/S1369-7021(05)70934-2.
[11] X.Q. Cao, R. Vassen, D. Stoever, Ceramic materials for thermal barrier coatings, Journal of the European Ceramic Society. 24 (2004) 1–10. https://doi.org/10.1016/S0955-2219(03)00129-8.
[12] W. Hu, Y. Lei, J. Zhang, J. Wang, Mechanical and thermal properties of RE4Hf3O12 (RE=Ho, Er, Tm) ceramics with defect fluorite structure, Journal of Materials Science & Technology. 35 (2019) 2064–2069.
[13] S.M. Lakiza, M.I. Hrechanyuk, V.P. Red'ko, O.K. Ruban, Ja.S. Tyshchenko, A.O. Makudera, O.V. Dudnik, The Role of Hafnium in Modern Thermal Barrier Coatings, Powder Metallurgy and Metal Ceramics. 60 (2021) 78–89. https://doi.org/10.1007/s11106-021-00217-1.
[14] D.L. Poerschke, C.G. Levi, Effects of cation substitution and temperature on the interaction between thermal barrier oxides and molten CMAS, Journal of the European Ceramic Society. 35 (2015) 681–691. https://doi.org/10.1016/j.jeurceramsoc.2014.09.006.
[15] D. Zhu, N.P. Bansal, R.A. Miller, Thermal Conductivity and Stability of $HfO_2 - Y_2O_3$ and $La_2Zr_2O_7$ Evaluated for 1650°C Thermal/Environmental Barrier Coating Applications, in: Ceramic Transactions Series, John Wiley & Sons, Inc., 2012: pp. 329–343. https://doi.org/10.1002/9781118406892.ch23.
[16] X. Luo, W. Zhou, S.V. Ushakov, A. Navrotsky, A.A. Demkov, Monoclinic to tetragonal transformations in hafnia and zirconia: A combined calorimetric and density functional study, Physical Review B. 80 (2009) 134119. https://doi.org/10.1103/PhysRevB.80.134119.
[17] B.M. Hudak, S.W. Depner, G.R. Waetzig, A. Talapatra, R. Arroyave, S. Banerjee, B.S. Guiton, Real-time atomistic observation of structural phase transformations in individual hafnia nanorods, Nature Communications. 8 (2017) 1–9. https://doi.org/10.1038/ncomms15316.

[18] M.H. Bocanegra-Bernal, S. Diaz, Phase transitions in zirconium dioxide and related materials for high performance engineering ceramics, Journal of Materials Science. 37 (2002) 4947–4971. https://doi.org/10.1023/A:1021099308957.

[19] J. Wang, H.P. Li, R. Stevens, Hafnia and hafnia-toughened ceramics, Journal of Materials Science. 27 (1992) 5397–5430. https://doi.org/10.1007/BF00541601.

[20] M.F. Trubelja, V.S. Stubican, Ionic Conductivity of the Fluorite-Type Hafnia-R2O3 Solid Solutions, Journal of the American Ceramic Society. 74 (1991) 2489–2494. https://doi.org/10.1111/j.1151-2916.1991.tb06790.x.

[21] K.K. Yadav, A. Gupta, M. Sharma, N. Dabas, A.K. Ganguli, M. Jha, Low temperature synthesis process of stabilization of cubic yttria stabilized zirconia spindles: an important high temperature ceramic material, Materials Research Express. 4 (2017) 105044. https://doi.org/10.1088/2053-1591/aa9231.

[22] V.V. Rodaev, S.S. Razlivalova, A.I. Tyurin, A.O. Zhigachev, Y.I. Golovin, Microstructure and Phase Composition of Yttria-Stabilized Zirconia Nanofibers Prepared by High-Temperature Calcination of Electrospun Zirconium Acetylacetonate/Yttrium Nitrate/Polyacrylonitrile Fibers, Fibers. 7 (2019) 82. https://doi.org/10.3390/fib7100082.

[23] A. Kulkarni, Z. Wang, T. Nakamura, S. Sampath, A. Goland, H. Herman, J. Allen, J. Ilavsky, G. Long, J. Frahm, R.W. Steinbrech, Comprehensive microstructural characterization and predictive property modeling of plasma-sprayed zirconia coatings, Acta Materialia. 51 (2003) 2457–2475. https://doi.org/10.1016/S1359-6454(03)00030-2.

[24] Y. Zhao, L. Wang, J. Yang, D. Li, X. Zhong, H. Zhao, F. Shao, S. Tao, Thermal Aging Behavior of Axial Suspension Plasma-Sprayed Yttria-Stabilized Zirconia (YSZ) Thermal Barrier Coatings, Journal of Thermal Spray Technology. 24 (2015) 338–347. https://doi.org/10.1007/s11666-014-0206-y.

[25] F. Fonseca, Analysis of the formation of ZrO2:Y2O3 solid solution by the electrochemical impedance spectroscopy technique, Solid State Ionics. 149 (2002) 309–318. https://doi.org/10.1016/S0167-2738(02)00184-4.

[26] S.Z. Othman, S. Ramesh, W.D. Teng, Sintering of Commercial Yttria-Stabilized Zirconia, Engineering e-Transaction. 1 (2006) 14–18.

[27] J.F. Bartolome, I. Montero, M. Diaz, S. Lopez-Esteban, J.S. Moya, S. Deville, L. Gremillard, J. Chevalier, G. Fantozzi, Accelerated Aging in 3-mol%-Yttria-Stabilized Tetragonal Zirconia Ceramics Sintered in Reducing Conditions, Journal of the American Ceramic Society. 87 (2004) 2282–2285. https://doi.org/10.1111/j.1151-2916.2004.tb07505.x.

[28] H.-C. Kim, I.-J. Shon, I.-K. Jeong, I.-Y. Ko, Z.A. Munir, Sintering of ultra-fine tetragonal yttria-stabilized zirconia ceramics, Journal of Materials Science. 42 (2007) 9409–9414. https://doi.org/10.1007/s10853-007-1888-z.

[29] J. D. Buckley, D. R. Wilder, Effects of cyclic heating and thermal shock on hafnia stabilized with calcia, magnesia, and yttria, No. NASA-TN-D-5279. (1969).

[30] C. Li, C. Ren, Y. Ma, J. He, H. Guo, Effects of rare earth oxides on microstructures and thermo-physical properties of hafnia ceramics, Journal of Materials Science & Technology. 72 (2021) 144–153. https://doi.org/10.1016/j.jmst.2020.07.031.

[31] P. Simoncic, A. Navrotsky, Energetics of rare-earth-doped hafnia, Journal of Materials Research. 22 (2007) 876–885. https://doi.org/10.1557/jmr.2007.0133.

[32] M. Yokoyama, T. Ota, I. Yamai, Flux growth of rare-earth stabilized zirconia and hafnia crystals, Journal of Crystal Growth. 94 (1989) 287–292. https://doi.org/10.1016/0022-0248(89)90001-8.

[33] K.E. Sickafus, R.W. Grimes, J.A. Valdez, A. Cleave, M. Tang, M. Ishimaru, S.M. Corish, C.R. Stanek, B.P. Uberuaga, Radiation-induced amorphization resistance and radiation tolerance in structurally related oxides, Nature Materials. 6 (2007) 217–223. https://doi.org/10.1038/nmat1842.

[34] C.V. Ramana, M. Noor-A-Alam, J.J. Gengler, J.G. Jones, Growth, Structure, and Thermal Conductivity of Yttria-Stabilized Hafnia Thin Films, ACS Applied Materials & Interfaces. 4 (2012) 200–204. https://doi.org/10.1021/am2012596.

[35] W. Zhou, S.V. Ushakov, A. Navrotsky, Yttria-stabilized hafnia: Thermochemistry of formation and hydration of nanoparticles, Journal of Materials Research. 27 (2012) 1022–1028. https://doi.org/10.1557/jmr.2012.31.

[36] H.U. Kessel, J. Hennicke, J. Schmidt, T. Weißgärber, B.F. Kieback, M. Herrmann, J. Räthel, “FAST” field assisted sintering technology- a new process for the production of metallic and ceramic sintering materials, Pulvermetallurgie in Wissenschaft Und Praxis. 22 (2008) 1–37.

[37] K. Morita, B.-N. Kim, H. Yoshida, K. Hiraga, Y. Sakka, Distribution of carbon contamination in oxide ceramics occurring during spark-plasma-sintering (SPS) processing: II - Effect of SPS and loading temperatures, Journal of the European Ceramic Society. 38 (2018) 2596–2604. https://doi.org/10.1016/j.jeurceramsoc.2017.12.004.

[38] É.S. Dvilis, V.D. Paigin, S.A. Stepanov, O.L. Khasanov, D.T. Valiev, E.F. Polisadova, V. Vaganov, T.R. Alishin, D.V. Dudina, Effect of Spark Plasma Sintering Temperature on the Properties of Transparent YSZ Ceramics, Refractories and Industrial Ceramics. 60 (2019) 154–159. https://doi.org/10.1007/s11148-019-00327-9.

[39] A. Fregeac, F. Ansart, S. Selezneff, C. Estournès, Relationship between mechanical properties and microstructure of yttria stabilized zirconia ceramics densified by spark plasma sintering, Ceramics International. 45 (2019) 23740–23749. https://doi.org/10.1016/j.ceramint.2019.08.090.

[40] G. Bernard-Granger, C. Guizard, Spark plasma sintering of a commercially available granulated zirconia powder: I. Sintering path and hypotheses about the mechanism(s) controlling densification, Acta Materialia. 55 (2007) 3493–3504. https://doi.org/10.1016/j.actamat.2007.01.048.

[41] P. T. B. Polla, M. I. Valentini, N. V. Junior, M. A. C. Berton, L. da Conceição, Evaluation of electrical conductivity and density of 8 mol% yttria-stabilized zirconia produced by Spark Plasma Sintering, Blucher Chemistry Proceedings. 4 (2016) 123–135.

[42] V. Tyrpekl, M. Holzhäuser, H. Hein, J.F. Vigier, J. Somers, Synthesis of dense yttrium-stabilised hafnia pellets for nuclear applications by spark plasma sintering, Journal of Nuclear Materials. 454 (2014) 398–404. https://doi.org/10.1016/j.jnucmat.2014.08.029.

[43] B.P. Mandal, N. Garg, S.M. Sharma, A.K. Tyagi, Preparation, XRD and Raman spectroscopic studies on new compounds RE2Hf2O7 (RE=Dy, Ho, Er, Tm, Lu, Y): Pyrochlores or defect-fluorite?, Journal of Solid State Chemistry. 179 (2006) 1990–1994. https://doi.org/10.1016/j.jssc.2006.03.036.

[44] Y. Ji, D. Jiang, T. Fen, J. Shi, Fabrication of transparent La2Hf2O7 ceramics from combustion synthesized powders, Materials Research Bulletin. 40 (2005) 553–559. https://doi.org/10.1016/j.materresbull.2004.10.010.

[45] Z. Wang, G. Zhou, D. Jiang, S. Wang, Recent development of A2B2O7 system transparent ceramics, Journal of Advanced Ceramics. 7 (2018) 289–306. https://doi.org/10.1007/s40145-018-0287-z.

[46] G. Caglioti, A. Paoletti, F.P. Ricci, Choice of collimators for a crystal spectrometer for neutron diffraction, Nuclear Instruments. 3 (1958) 223–228. https://doi.org/10.1016/0369-643X(58)90029-X.

[47] H. Toraya, A new method for quantitative phase analysis: Direct derivation of weight fractions from observed intensities and chemical composition data of individual crystalline phases, Rigaku Journal. 34 (2018) 3–8. https://doi.org/10.1107/S1600576716010451.

[48] W. Li, L. Gao, Rapid sintering of nanocrystalline ZrO2(3Y) by spark plasma sintering, Journal of the European Ceramic Society. 20 (2000) 2441–2445. https://doi.org/10.1016/S0955-2219(00)00152-7.

[49] A. Flaureau, A. Weibel, G. Chevallier, C. Estournès, Study of the densification and grain growth mechanisms occurring during spark plasma sintering of different submicronic yttria-stabilized zirconia powders, Journal of the European Ceramic Society. 41 (2021) 3581–3594. https://doi.org/10.1016/j.jeurceramsoc.2021.01.032.

[50] A. Moradkhani, H. Baharvandi, A. Naserifar, Effect of Sintering Temperature on the Grain Size and Mechanical Properties of Al2O3-SiC Nanocomposites, Journal of the Korean Ceramic Society. 56 (2019) 256–268. https://doi.org/10.4191/kcers.2019.56.3.01.

[51] J. Zhao, Y. Zhang, H. Gong, Y. Zhang, X. Wang, X. Guo, Y. Zhao, Fabrication of high-performance Y2O3 stabilized hafnium dioxide refractories, Ceramics International. 41 (2015) 5232–5238. https://doi.org/10.1016/j.ceramint.2015.01.047.

[52] E. Serrano Pérez, H. Martinez Gutierrez, K.J. Martinez Gonzalez, E. Marín Moares, F. Juárez López, Densification and microstructure of spark plasma sintered 7YSZ–Gd_2O_3 ceramic nano-composites, Journal of Asian Ceramic Societies. 5 (2017) 266–275. https://doi.org/10.1016/j.jascer.2017.05.004.

[53] D.W. Stacy, D.R. Wilder, The Yttria-Hafnia System, Journal of the American Ceramic Society. 58 (1975) 285–288. https://doi.org/10.1111/j.1151-2916.1975.tb11476.x.

[54] M. Yashima, N. Ishizawa, M. Yoshimura, Application of an Ion-Packing Model Based on Defect Clusters to Zirconia Solid Solutions: II, Applicability of Vegard's Law, Journal of the American Ceramic Society. 75 (1992) 1550–1557. https://doi.org/10.1111/j.1151-2916.1992.tb04223.x.

[55] T.A. Lee, A. Navrotsky, Enthalpy of formation of cubic yttria-stabilized hafnia, Journal of Materials Research. 19 (2004) 1855–1861. https://doi.org/10.1557/JMR.2004.0234.

[56] J. Janek, C. Korte, Electrochemical blackening of yttria-stabilized zirconia – morphological instability of the moving reaction front, Solid State Ionics. 116 (1999) 181–195. https://doi.org/10.1016/S0167-2738(98)00415-9.

[57] M. Fattahi, A. Mohammadzadeh, Y. Pazhouhanfar, S. Shaddel, M. Shahedi Asl, A. Sabahi Namini, Influence of SPS temperature on the properties of TiC–SiCw composites, Ceramics International. 46 (2020) 11735–11742. https://doi.org/10.1016/j.ceramint.2020.01.206.